Properties of Randomly Distributed Sparse Acoustic Sensors for Ground Vehicle Tracking and Localization

M. R. Azimi-Sadjadi*[a], Y. Jiang [b] and G. Wichern [c] †

[a]Information System Technologies, Inc.
Fort Collins, CO, 80521
[b]Department of Electrical and Computer Engineering
University of Colorado, Boulder, CO 80309
[c]Electrical and Computer Engineering Department
Colorado State University, Fort Collins, CO, 80523

ABSTRACT

In order to resolve multiple closely spaced sources moving in a tight formation using unattended acoustic sensors, the array aperture must be extended using a sparse array geometry. Traditional sparse array algorithms rely on the spatial invariance property often leading to inaccurate Direction of Arrival (DOA) estimates due to the large side-lobes present in the power spectrum. Many problems of traditional sparse arrays can be alleviated by forming a sparse array using randomly distributed single microphones. The power spectrum of a random sparse array will almost always exhibit low side-lobes, thus increasing the ability of the beamforming algorithm to accurately separate and localize sources. This paper examines the robustness of randomly distributed sparse array beamforming in situations where the exact sensor location is unknown and benchmark its performance with that of traditional baseline sparse arrays. We will also use a realistic acoustic propagation model to study fading effects as a function of range and its effects on the beamforming process for various sparse array configurations.

Keywords: Distributed Acoustic Sensor Networks, Sparse Array Processing, Capon Beamforming, Sensor Location Uncertainty, Acoustic Transmission Loss

1. INTRODUCTION

The emergence of small, low cost and low-power sensor technologies that possess on-board signal processing and wireless communication capabilities has stimulated great interests in utilization of distributed sensor networks in a wide variety of applications. These distributed sensor networks offer a new and promising paradigm for military surveillance, reconnaissance and situation awareness such as military operations in urban terrain (MOUT).[1] Additionally, there has been considerable attention to develop miniature sensitive microphones for many new industrial and military applications that require acoustic data collection over larger bandwidths for proper signal detection and identification. These microphones can operate in harsh environments and measure a wide range of sound pressure levels.

In distributed sensor processing a group of sensor nodes form a cluster responsible to detect and recognize a locally occurring event recorded by most of, if not all, the nodes in the cluster. Some preliminary detection, feature extraction and lossy compression is often carried out at node-level and only the essential information is broadcast to the gateway or the master station at which the high level decisions such as target localization, tracking and classification takes place. In this framework, intra-cluster communication among nodes is possible due to small distances between the nodes within a cluster. This allows for collaborative signal processing among certain nodes in a cluster. However, this requires complicated sensor management strategies. Clearly, there are several advantages of distributed versus centralized processing that include reduce bandwidth and power requirements, reduced computations at the master station, and hence reduced costs. Nevertheless, the main disadvantage is that the master station has access to only partial information transmitted by the sensor nodes, which may result in loss of performance.

*mo@infsyst.biz; phone: 1 970 224 2556; http://www.infsyst.com.
†Y. Jiang and and G. Wichern are consultants at Information System Technologies, Inc.

In[2] we investigated several important properties of the randomly distributed acoustic sensors for detection, tracking and localization of moving sources namely vehicles. More specifically, direction of arrival (DOA) estimation accuracy and resolution for separating multiple closely spaced sources, robustness to noise, and effects of node/array placement on the beampattern and bearing response of the Capon beamformer for these sparse arrays were carefully studied and benchmarked against baseline 5-element wagon-wheel sensor arrays. Although these studies were conducted using synthetically generated narrowband sources, the results can directly be applicable to wideband sources as well. The results of these experiments led to several intriguing conclusions. As far as DOA resolution is concerned sparse distributed arrays provide much better ability in separating closely spaced sources than a single baseline array. However, sparse arrays formed of multiple baseline arrays exhibit dramatic deterioration in DOA accuracy when the sources are near-field. That is, the effect of array steering mismatch (actual versus presumed) caused by near-field or wavefront perturbation effects has more dramatic impact on the baseline arrays due to prominent and regular side-lobe structure of these arrays.

In this paper, we further investigate the properties of the distributed sensor arrays in terms of their robustness to array mismatch caused by sensor location errors and acoustic transmission loss. Comparison with sparse arrays made of several baseline arrays is also made. Simulation results are also provided to further evaluate the various sparse array configurations.

2. SPARSE ARRAY CONFIGURATIONS AND PROPERTIES

In this section, two different sparse array configurations are considered and thoroughly studied. These are: sparse arrays consisting of several 5-element wagon-wheel nodes and sparse randomly distributed single microphones that exhibit frequency diversity. In the following subsection, we first review the sparse DOA processing for the regular 5-element sparse configuration.

2.1. Baseline Versus Random Distributed Sparse Arrays

Here we refer to *baseline sparse arrays* as those formed of several typical wagon-wheel 5-element subarrays/nodes placed at different distance from each other. On the other hand, a randomly distributed sparse array consists of multiple single microphone nodes with no particular structure. For example Figure 1 shows a baseline sparse array consisting of three five-element wagon wheel subarrays/nodes. The idea behind multiple invariance[3,4] is used for baseline sparse arrays in order to develop an efficient array processing algorithm.

For the geometry in Figure 1, the array measurement vector for node 1 (reference 5-element subarray) at frequency f_j and over a fixed time snapshot may be expressed as

$$\mathbf{x}_1(f_j) = \mathrm{A}_1(f_j, \boldsymbol{\theta}_1)\mathbf{s}(f_j) + \mathbf{n}_1(f_j) \tag{1}$$

where $\mathbf{s}(f_j) = [s_1(f_j), \ldots, s_d(f_j)]$ represents the vector of d narrow-band source signals at frequency f_j, $\mathbf{n}_1(f_j)$ is the measurement noise vector for node 1 at frequency f_j, and

$$\mathrm{A}_1(f_j, \boldsymbol{\theta}_i) = [\mathbf{a}_1(f_j, \theta_{1,1}), \ldots, \mathbf{a}_1(f_j, \theta_{1,d})] \in C^{5\times d} \tag{2}$$

is the array steering matrix for node 1 at frequency f_j that steers to d plane-waves at angles $\boldsymbol{\theta}_1 = [\theta_{1,1}, \ldots, \theta_{1,d}]^T$. Therefore, the lth steering vector of node 1 may be written as

$$\mathbf{a}_1(f_j, \theta_{1,l}) = [1, e^{j\frac{2\pi f_j r}{c}\sin(\theta_{1,l})}, e^{j\frac{2\pi f_j r}{c}\cos(\theta_{1,l})}, e^{-j\frac{2\pi f_j r}{c}\sin(\theta_{1,l})}, e^{-j\frac{2\pi f_j r}{c}\cos(\theta_{1,l})}]^T/\sqrt{5} \in C^{5\times 1} \tag{3}$$

where r is the radius of each wagon-wheel array and c is the speed of sound in air.

Assume that the sources are far field so that the angles at nodes 1, 2 and 3 are almost equal, i.e. $\boldsymbol{\theta} = \boldsymbol{\theta}_1 \approx \boldsymbol{\theta}_2 \approx \boldsymbol{\theta}_3$. This far field assumption is the fundamental assumption behind almost all sparse processing methods that are based on the idea of multiple invariance.[3,4] Using this assumption and the geometry of the sparse array configuration in Figure 1, it may easily be shown that the array steering matrices at different nodes have the following translation invariance property:

$$\mathrm{A}_i(f_j, \boldsymbol{\theta}) = \mathrm{A}_1(f_j, \boldsymbol{\theta})\Phi_i(f_j, \boldsymbol{\theta}); \quad \text{for } i = 2, \text{ and } 3 \tag{4}$$

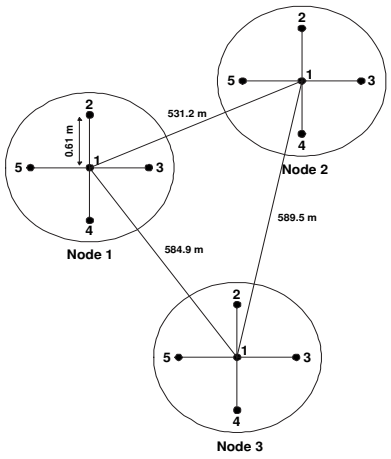

Figure 1. A sparse configuration with three 5-element wagon wheel subarrays.

with $\Phi_i(f_j, \boldsymbol{\theta}) = Diag[e^{-j\frac{2\pi f_j}{c}(x_i sin(\theta_1)+y_i cos(\theta_1))} \cdots e^{-j\frac{2\pi f_j}{c}(x_i sin(\theta_d)+y_i cos(\theta_d))}]$ where x_i and y_i are the distances between node i and node 1 along the $x-$ and $y-$axes, respectively, assuming that node 1 is positioned at the origin of the coordinate system. Using this invariance property, we may define the augmented array steering matrix $\mathrm{A}(f_j, \boldsymbol{\theta})$, consisting of the array steering matrices of a subset or all the nodes, along with their corresponding augmented array measurement vector $\mathbf{z}(f_j)$. For the three-node array case, as shown in Figure 1, we can write

$$\mathrm{A}(f_j, \boldsymbol{\theta}) = \begin{bmatrix} \mathrm{A}_1(f_j, \boldsymbol{\theta}) \\ \mathrm{A}_2(f_j, \boldsymbol{\theta}) \\ \mathrm{A}_3(f_j, \boldsymbol{\theta}) \end{bmatrix} = \begin{bmatrix} \mathrm{A}_1(f_j, \boldsymbol{\theta}) \\ \mathrm{A}_1(f_j, \boldsymbol{\theta})\Phi_2(f_j, \boldsymbol{\theta}) \\ \mathrm{A}_1(f_j, \boldsymbol{\theta})\Phi_3(f_j, \boldsymbol{\theta}) \end{bmatrix} \tag{5}$$

and

$$\mathbf{x}(f_j) = [\mathbf{x}_1^H(f_j) \quad \mathbf{x}_2^H(f_j) \quad \mathbf{x}_3^H(f_j)]^H \tag{6}$$

The augmented measurement vector $\mathbf{x}(f_j)$ may be viewed as an array measurement vector recorded by a larger array with steering matrix $\mathrm{A}(f_j, \boldsymbol{\theta})$. In other words, $\mathbf{x}(f_j)$ and $\mathrm{A}(f_j, \boldsymbol{\theta})$ are regarded as the measurement vector and steering matrix for a single large array, and hence all the standard beamforming and DOA estimation methods[5] may be applied to them in order to estimate the angles $\boldsymbol{\theta} = [\theta_1, \ldots, \theta_d]^T$. For example, we may use the Capon beamforming method[5] to estimate the angles:

$$P_{\mathrm{Capon}}(f_j, \theta_l) = \frac{1}{\mathbf{a}^H(f_j, \theta_l)\mathrm{R}_{xx}^{-1}(f_j)\mathbf{a}(f_j, \theta_l)} \tag{7}$$

where $P_{\mathrm{Capon}}(f_j, \theta_l)$ is the true Capon power spectrum, $\mathbf{a}(f_j, \theta_l)$ is the lth column of $\mathrm{A}(f_j, \boldsymbol{\theta})$, and $\mathrm{R}_{xx}(f_j) = E[\mathbf{x}(f_j)\mathbf{x}^H(f_j)]$ is the true covariance matrix of $\mathbf{x}(f_j)$.

In practice, however, where only a limited number of samples are available, the true covariance matrix can be replaced by the sample covariance matrix $\hat{\mathrm{R}}_{xx}(f_j) = \frac{1}{K}\sum_{k=1}^{K}\mathbf{x}(f_j, k)\mathbf{x}(f_j, k)^H$ where $\mathbf{x}(f_j, k)$ is the sample at snapshot k. This leads to the "practical" Capon power

$$\hat{P}_{\mathrm{Capon}}(f_j, \theta_l) = \frac{1}{\mathbf{a}^H(f_j, \theta_l)\hat{\mathrm{R}}_{xx}^{-1}(f_j)\mathbf{a}(f_j, \theta_l)}. \tag{8}$$

This practical Capon power spectrum is related to the theoretical one in (7) using

$$\hat{P}_{\mathrm{Capon}}(f, \theta) = P_{\mathrm{Capon}}(f, \theta)\eta(\theta) \tag{9}$$

for any frequency f and angle θ. Here $\eta(\theta)$ is a random variable with scaled Chi square distribution:

$$f_{\eta(\theta)}(x) = \frac{K^{K-M+1}}{(K-M)!} x^{K-M} e^{-Kx}, \quad x \geq 0. \tag{10}$$

where M is the number of sensors in the array. The proof is omitted here. We note that although $\eta(\theta)$ has the distribution independent of θ, the specific realizations of $\eta(\theta)$ are different for different θ. If $K - M \gg 1$, then with high probability, $\eta(\theta)$ concentrate around one. As $K - M \to \infty$, $\eta(\theta) \to 1$ in probability. In our numerical experiments, $M = 15$ (15 sensors) and $K = 1024$, hence $K - M \gg 1$. Thus, in the subsequent discussions, we use the theoretical Capon power spectrum instead of the practical one. Additionally, without loss of generality, we assume unit noise power, i.e. $E[\mathbf{n}\mathbf{n}^H] = I$.

To simplify our discussions let us now consider the case where only a single source is present with DOA θ_0 and signal power P_s. Thus, the covariance matrix of the recorded signal $\mathbf{x}(f)$ becomes $\mathrm{R}_{xx}(f) = \mathbf{a}(f,\theta_0)\mathbf{a}^H(f,\theta_0)P_s(f) + I$. Inserting this into the expression for the theoretical Capon power spectrum (7) and applying the matrix inversion lemma yields

$$P_{\text{Capon}}(f,\theta) = \frac{1}{1 - \frac{P_s(f)}{1+P_s(f)}|\mathbf{a}^H(f,\theta)\mathbf{a}(f,\theta_0)|^2} \tag{11}$$

Clearly, the power spectrum is determined by the "Radiation Pattern" function[5] $P_{\text{RP}}(f,\theta) \triangleq |\mathbf{a}^H(f,\theta)\mathbf{a}(f,\theta_0)|$. As a result, in the single source case, the study of the radiation pattern function can provide us sufficient information on the power spectrum of the Capon beamformer for a particular array configuration.

As far as the sparse arrays formed of baseline 5-element nodes are concerned, the radiation pattern can be expressed[5] as

$$P(f,\theta) = P_1(f,\theta)P_2(f,\theta). \tag{12}$$

where $P_1(f,\theta) = |\mathbf{a}_1^H(f,\theta)\mathbf{a}_1(f,\theta_0)|$ and $P_2(f,\theta) = |\mathbf{a}_2^H(f,\theta)\mathbf{a}_2(f,\theta_0)|$ are the radiation patterns of one 5-element node and L-node array, respectively. For the 5-element node the steering vector is given in (3). If the sparse array is composed of L nodes, then $\mathbf{a}_2(f,\theta) = \left[e^{-j2\pi\frac{y_1\cos\theta + x_1\sin\theta}{\lambda}}, \ldots, e^{-j2\pi\frac{y_L\cos\theta + x_L\sin\theta}{\lambda}}\right]^T/\sqrt{L}$ where the center of the lth node is assumed to be at $\mathbf{p}_l = [x_l, y_l]^T$, $l = 1, \ldots, L$ and $\lambda = c/f$ is the wavelength.

To simplify the analysis we consider two different 5-element node array configurations with $L = 3$ as shown in Figure 2. We assume $r = \frac{\lambda}{2}$ and the true source DOA is at $\theta_0 = 0$. The plot of the radiation pattern $P_1(f,\theta)$ is shown in Figure 3. The radiation pattern $P_2(f,\theta)$ associated with the sparse array in Figure 2(a) is shown in Figure 4, where m is the number of the half-wavelength node separation distances as shown in Figure 2(a). Figure 6(a) shows the overall radiation pattern $P(f,\theta)$ as given by (12).

We set the center of mass of the equilateral triangle of Figure 2(b) as the origin point of Cartesian coordinate. It follows from the structure of $\mathbf{a}_2(f,\theta)$ that the steering vector associated with the sparse array configuration of Figure 2(b) is $\mathbf{a}_2(f,\theta) = \left[e^{-j\pi\frac{n\sin\theta}{\sqrt{3}}}, e^{-j\pi\left(\frac{(n\cos\theta}{2} - \frac{n\sin\theta}{2\sqrt{3})}\right)}, e^{j\pi\left(\frac{(n\cos\theta}{2} + \frac{n\sin\theta}{2\sqrt{3})}\right)}\right]^T$. The radiation pattern $P_2(f,\theta)$ associated with Figure 2(b) is shown in Figure 5, where n is the number of the half-wavelength node separation distances as shown in Figure 2(b). Figure 6(b) shows the overall radiation pattern $P(f,\theta)$ for this sparse array configuration.

Remark: From these results we clearly notice this important property of the radiation patterns: when the nodes are far away from each other, e.g., separated by distances greater than 25λ, then for both configurations in Figure 2 (around $\theta_0 = 0$) there are several side-lobes with amplitude near one. It follows from (11) that the Capon power spectrum also has several closely located peaks as shown in Figure 7. Clearly, the DOA estimates generated using the Capon beamformer are very sensitive to the perturbations such as background noise, finite

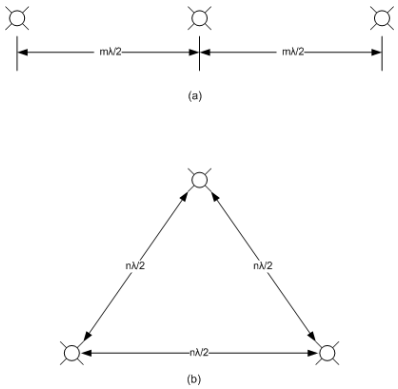

Figure 2. Two configurations with three 5-element nodes.

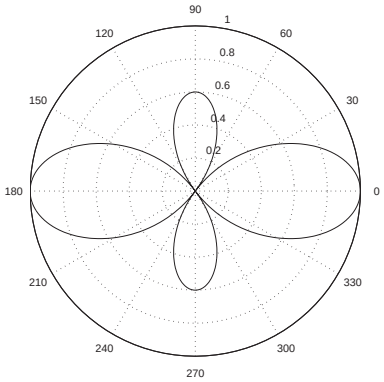

Figure 3. The radiation pattern of a 5-element node $P_1(f, \theta)$. $\theta_0 = 0$.

snapshot number, steering vector error, and model mismatch effects. The variability of the side-lobe structure with the distance between the nodes could become a major issue when there are uncertainties in the locations of the nodes.

Clearly, the main motivation behind multiple invariance arrays[3, 4] is to take advantage of various microphone spacings some of which are less than one-half wavelength of the source signal while the others are greater than one-half wavelength. In this way, for those groups of microphones that have spacings less than one-half

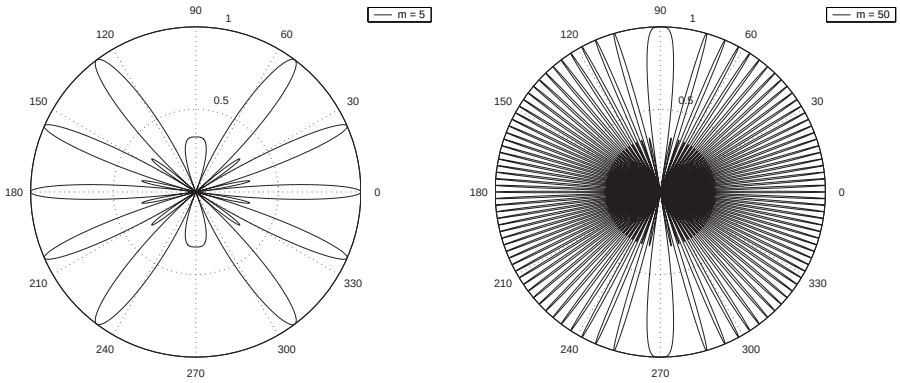

(a) m=5 (b) m=50

Figure 4. The radiation pattern $P_2(f, \theta)$ associated with the configuration of Figure 2(a) for two choices of m, $\theta_0 = 0$.

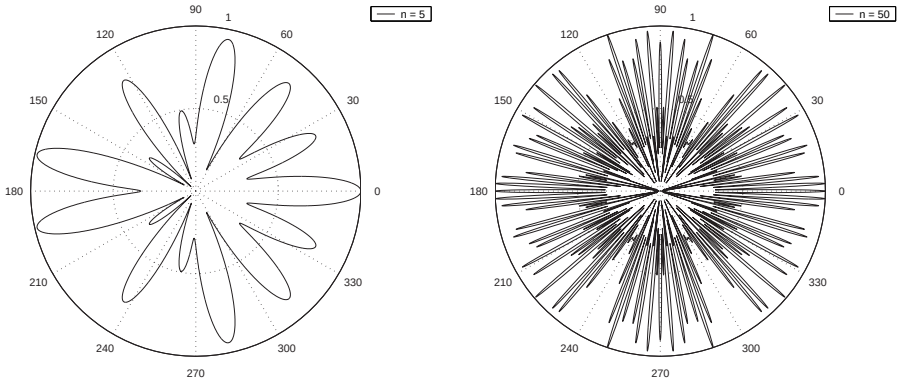

(a) n=5 (b)n=50

Figure 5. The radiation pattern $P_2(f, \theta)$ associated with the configuration of Figure 2(b) for two choices of n, $\theta_0 = 0$.

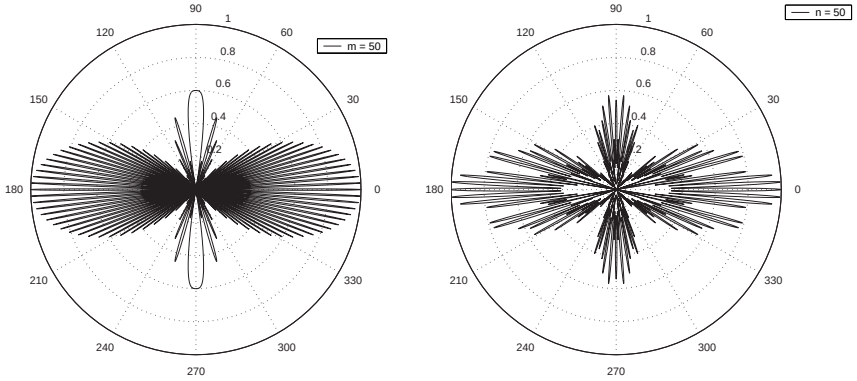

(a) (b)

Figure 6. The radiation pattern $P(f, \theta)$ of two baseline sparse array configurations. (a) Configuration of Figure 2(a) with $m = 50$. (b) Configuration of Figure 2(b) with $n = 50$.

wavelength of the source signal, coarse but unambiguous DOA estimates can be produced; whereas the sparsely located sub-arrays provide fine resolution for the DOA estimates at the cost of introducing ambiguity in form of the grating lobes. Thus, by combining both properties, the unambiguous coarse DOA estimates may be used to eliminate the ambiguities introduced by spatial aliasing.

As far as the random distributed sensor arrays are concerned the array steering matrix has no specific structure. Thus, for a narrowband far field source of frequency f and assuming an M-element distributed array, the steering vector is $\mathbf{a}(f, \theta) = [e^{j\phi_1(\theta)}, e^{j\phi_2(\theta)}, \ldots, e^{j\phi_M(\theta)}]^T/\sqrt{M}$. In the 2-D case,

$$\phi_i(\theta) = -\frac{2\pi}{\lambda}(x_i \sin\theta + y_i \cos\theta), \quad i = 1, 2, \ldots, M$$

is a function of the location of the ith sensor $\mathbf{p}_i = [x_i,\ y_i]$.

In contrast to the baseline sparse arrays, the power spectrum of the Capon beamformer for a distributed sensor array configuration does not exhibit any regular side-lobe structure. Example radiation patterns and power spectra of the Capon beamformer for distributed sparse arrays of 15 randomly placed microphones in a coverage area of $50\lambda \times 50\lambda$ will be presented in Section 3 (Figures 10 and 11). The main peaks associated with the true source locations tend to be easily distinguishable in the power spectra for randomly distributed arrays. This important property that the randomly distributed arrays do not have a regular grating lobe structure similar to those of the baseline arrays makes them more immune to DOA errors caused by various types of mismatches that are investigated in Section 3.

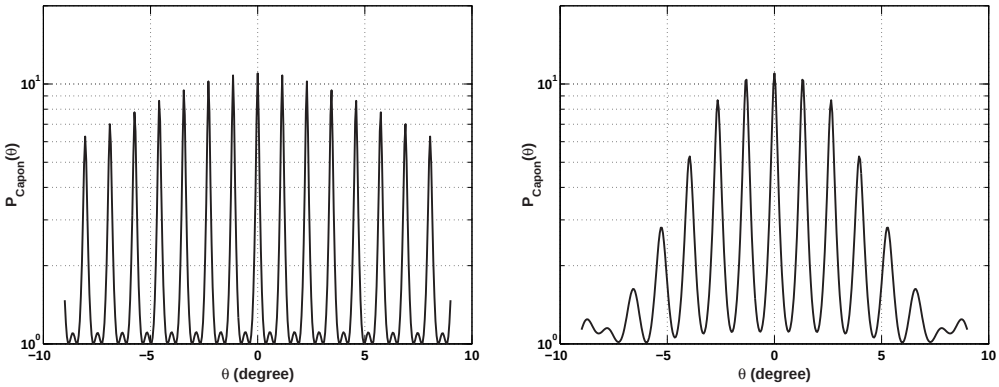

(a) (b)

Figure 7. The Capon power spectrum $P_{\text{Capon}}(f,\theta)$. $P_s(f) = 10, \theta_0 = 0$. (a) Configuration of Figure 2(a) with $m = 50$. (b) Configuration of Figure 2(b) with $n = 50$.

Remark: Note that although the treatment in this paper is primarily focused on narrowband sources, the same studies can be carried out for wideband sources. In this case, the power spectra at different frequencies may be averaged together to produce a wideband Capon bearing response. It has been shown[6] geometric average of narrowband output powers provides more accurate DOA estimates compared to arithmetic and harmonic averages. Thus, for the wideband case, we consider the following wideband Capon bearing response[6]

$$C(f,\theta_l) = \prod_{i=1}^{J} \frac{1}{\mathbf{a}^H(f_j,\theta_l)\mathrm{R}_{xx}^{-1}(f_j)\mathbf{a}(f_j,\theta_l)} \tag{13}$$

where J is the total number of narrowband frequency components.

3. ROBUSTNESS OF DIFFERENT SPARSE ARRAYS TO MODEL MISMATCHES

In the subsequent subsections, several studies are carried out in order to determine the performance of the two sparse array configurations in terms of DOA accuracy and robustness to sensor location error and sound transmission loss.

3.1. Sensor Location Uncertainties

In practice, the exact position of a sensor node in an array is known only up to a certain accuracy. This problem has become a major concern especially in large sensor networks due to the difficulties in accurate localization. When using a beamforming method to estimate target positions, these location uncertainties lead to phase errors in the steering vector, which in turn may lead to erroneous DOA estimates. In sparse array processing, the cumulative effect of these phase errors can be detrimental. In this study the effect of sensor location uncertainty and the resultant phase errors on different array configurations is studied.

In this section, we derive the radiation pattern of a sensor array in the presence of sensor location error. Suppose the nominal position of the ith ($i = 1, 2, \ldots, M$) sensor is $\mathbf{p}_i = [x_i,\ y_i]^T$, while the true position is $\mathbf{p}_i + \Delta\mathbf{p}_i = [x_i + \delta x_i,\ y_i + \delta y_i]^T$. We model the position errors $\{\delta x_i,\ \delta y_i\}_{i=1}^{M}$ as zero-mean Gaussian random variables with variance σ_p^2.

For the baseline sparse arrays made of L 5-element circular nodes, the location uncertainties are only assumed for the center of the nodes. That is, no sensor location error is considered for the five elements within each circular array itself. In this case, the steering vector is given by

$$\mathbf{a}(f,\theta) = [\mathbf{a}_1(f,\theta)e^{-j[(y_1+\delta y_1)\cos\theta+(x_1+\delta x_1)\sin\theta]}, \ldots, \mathbf{a}_1(f,\theta))e^{-j[(y_L+\delta y_L)\cos\theta+(x_L+\delta x_L)\sin\theta]}]^T/\sqrt{5L} \tag{14}$$

where $\mathbf{a}_1(f,\theta))$ is the 5-element array steering vector (3).

For the randomly distributed microphone arrays, location uncertainties are assumed for every sensor. The steering vector for the random sensor configuration with location uncertainties is given by,

$$\mathbf{a}(f,\theta) = [e^{-j[(y_1+\delta y_1)\cos\theta+(x_1+\delta x_1)\sin\theta]\frac{2\pi f}{\lambda}}, \ldots, e^{-j[(y_M+\delta y_M)\cos\theta+(x_M+\delta x_M)\sin\theta]\frac{2\pi}{\lambda}}]^T/\sqrt{M} \tag{15}$$

where M is the number of sensors in the randomly distributed array.

For a narrowband source of frequency f and DOA θ_0, the radiation pattern with location errors is

$$\mathrm{P}_{\mathrm{RP}}(f,\theta) = \left| \sum_{i=1}^{M} e^{j\frac{2\pi}{\lambda}(x_i\sin\theta+y_i\cos\theta)} e^{-j\frac{2\pi}{\lambda}[(x_i+\delta x_i)\sin\theta_0+(y_i+\delta y_i)\cos\theta_0]} \right|. \tag{16}$$

The array gain at the steering direction θ_0 is

$$G_a = \sum_{i=1}^{M} e^{-j\frac{2\pi}{\lambda}(\delta x_i\sin\theta_0+\delta y_i\cos\theta_o)}$$

If there is no sensor displacement, then $G_a = M$. But in presence of sensor location error, G_a is a random variable with mean

$$E[G_a] = E\left[\sum_{i=1}^{M} e^{-j\frac{2\pi}{\lambda}(\delta x_i\sin\theta_0+\delta y_i\cos\theta_o)}\right] = ME\left[e^{-j\frac{2\pi}{\lambda}(\delta x_i\sin\theta_0+\delta y_i\cos\theta_o)}\right],$$

where

$$E\left[e^{-j\frac{2\pi}{\lambda}(\delta x_i\sin\theta_0+\delta y_i\cos\theta_o)}\right] = \int_{-\infty}^{\infty} e^{-j\frac{2\pi}{\lambda}x}\frac{1}{\sqrt{2\pi\sigma_p^2}}e^{-\frac{x^2}{2\sigma_p^2}}dx = e^{-\frac{2\pi^2\sigma_p^2}{\lambda^2}}. \tag{17}$$

From (17), we can readily see that to make the gain loss less than 3 dB, σ_p^2 should be no more than $\frac{\ln\sqrt{2}}{2\pi^2}\lambda^2 = 0.0176\lambda^2$. If $\sigma_p = \lambda$, then the gain loss due to position error is more than 170 dB, and hence the array usually will not work at all.

In the following, we derive $E\left\{\mathrm{P}_{\mathrm{RP}}^2(f,\theta)\right\}$ to examine the effects of location uncertainties on the radiation pattern. According to (16),

$$\begin{aligned}
E\left\{\mathrm{P}_{\mathrm{RP}}^2(f,\theta)\right\} &= E\left\{\sum_{i=1}^{M}\sum_{l=1}^{M} e^{j\frac{2\pi}{\lambda}(x_i\sin\theta+y_i\cos\theta)} e^{-j\frac{2\pi}{\lambda}[(x_i+\delta x_i)\sin\theta_0+(y_i+\delta y_i)\cos\theta_0]}\right. \\
&\qquad \left. e^{-j\frac{2\pi}{\lambda}(x_l\sin\theta+y_l\cos\theta)} e^{j\frac{2\pi}{\lambda}[(x_l+\delta x_l)\sin\theta_0+(y_l+\delta y_l)\cos\theta_0]}\right\} \qquad (18) \\
&= \sum_{i=1}^{M}\sum_{l=1}^{M} E\left\{e^{j\frac{2\pi}{\lambda}(x_i\sin\theta+y_i\cos\theta)} e^{-j\frac{2\pi}{\lambda}[(x_i+\delta x_i)\sin\theta_0+(y_i+\delta y_i)\cos\theta_0]}\right. \\
&\qquad \left. e^{-j\frac{2\pi}{\lambda}(x_l\sin\theta+y_l\cos\theta)} e^{j\frac{2\pi}{\lambda}[(x_l+\delta x_l)\sin\theta_0+(y_l+\delta y_l)\cos\theta_0]}\right\} \qquad (19) \\
&= \sum_{i=1}^{M}\sum_{l=1}^{M} e^{j\frac{2\pi}{\lambda}(x_i\sin\theta+y_i\cos\theta)} e^{-j\frac{2\pi}{\lambda}(x_i\sin\theta_0+y_i\cos\theta_0)} e^{-j\frac{2\pi}{\lambda}(x_l\sin\theta+y_l\cos\theta)} e^{j\frac{2\pi}{\lambda}(x_l\sin\theta_0+y_l\cos\theta_0)} \\
&\qquad E\left\{e^{j\frac{2\pi}{\lambda}[(\delta x_l\sin\theta_0+\delta y_l\cos\theta_0)-(\delta x_i\sin\theta_0+\delta y_i\cos\theta_0)]}\right\}. \qquad (20)
\end{aligned}$$

Denote $a_{il} = E\left\{e^{j\frac{2\pi}{\lambda}[(\delta x_l\sin\theta_0+\delta y_l\cos\theta_0)-(\delta x_i\sin\theta_0+\delta y_i\cos\theta_0)]}\right\}$, then

$$a_{il} = \begin{cases} 1 & i = l \\ e^{-\frac{4\pi^2\sigma_p^2}{\lambda^2}} & i \neq l \end{cases}. \tag{21}$$

Then (20) can be shown to be[5]

$$E\left\{\mathrm{P}_{\mathrm{RP}}^2(f,\theta)\right\} = |\mathbf{a}(f,\theta)^*\mathbf{a}(f,\theta_0)|^2 e^{-\frac{4\pi^2\sigma_p^2}{\lambda^2}} + M\left(1 - e^{-\frac{4\pi^2\sigma_p^2}{\lambda^2}}\right). \tag{22}$$

Equation (22) clearly shows that the effects of sensor location error on the radiation pattern is two-fold. First, the radiation pattern is attenuated uniformly by a factor of $e^{-\frac{4\pi^2\sigma_p^2}{\lambda^2}}$ as shown in the first term of (22). Second, the side-lobe level is increased by $M\left(1 - e^{-\frac{4\pi^2\sigma_p^2}{\lambda^2}}\right)$.

The array gain degradation due to position error is shown in Figure 8. We note that the gain degradation is only a function of σ_p^2 and is independent of the array configuration. Figure 9(a) shows the mean-squared-error (MSE) of DOA estimation using the Capon estimator, where M sensors are randomly distributed in a $50\lambda \times 50\lambda$ area according to a uniform distribution. We find that the Capon estimator works well when the position error is less than a threshold. This is because when σ_p reaches some threshold, the array gain is so severely degraded that the main-lobe disappears. Moreover, the threshold is larger for a larger number of sensors, M. When M is large, the array gain is large hence the main-lobe can survive more severe sensor displacement. *Thus, we can conclude that the large sensor array is more robust against the location error.*

In Figure 9(b), we compare the MSE's of the Capon estimator using a uniformly distributed random array and three 5-element arrays with the configuration shown in Figure 2(a). We see from Figure 9(b) that the random array has better DOA estimation performance when $\sigma_p \leq 0.25\lambda$. In particular, when there is no position error, the 5-element array has inferior performance due to high side-lobes as shown in Figure 7(a). In contrast, the random array has low side-lobes with high probability.[9,10] When $\sigma_p > 0.25\lambda$, the 5-element node array seems to have more accurate DOA estimates. However, under this circumstance, both arrays have MSE values of more than 20, which are not good enough to provide meaningful estimates.

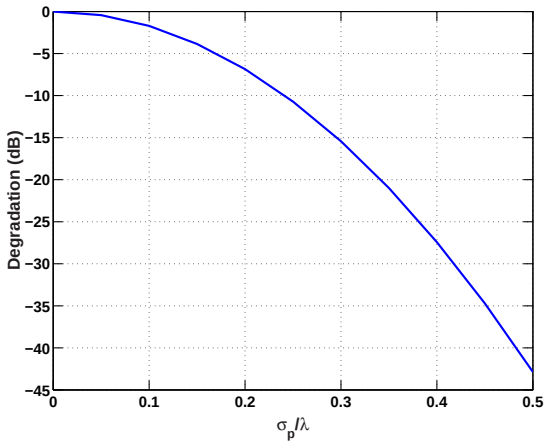

Figure 8. Array gain degradation due to position error.

3.2. Acoustic Transmission Loss

Acoustic transmission loss can have dramatic impact on DOA estimation and source separation. While the sensor location uncertainties and near-field effects cause phase errors or mismatches to the presumed steering vector, the transmission loss is equivalent to incorporating magnitude errors (fading effects) to the elements of the steering vector. Due to the large spacing between sensors in sparse array processing, the effects of acoustic transmission loss become increasingly important in these problems. In this section, we study the effect of this transmission loss on DOA estimation accuracy for different sparse array configurations.

When the distance between the acoustic sensors of an array is large, it is possible for different sensors to have different values of SNR, i.e., sensors closer to the source will have larger SNR when compared to those

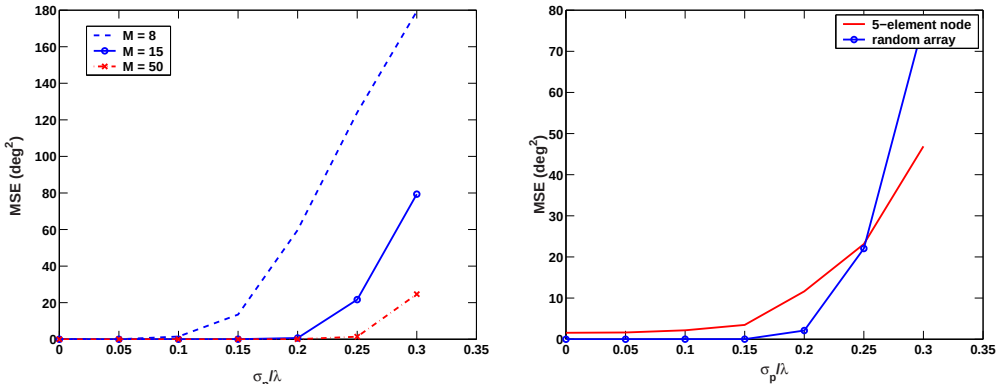

(a) (b)

Figure 9. DOA estimation degradation with respect to position error.

farther from the source. To study the effects of transmission loss on the Capon beamformer we no longer assume unit power for the measurement noise of all sensors, rather different noise power for each sensor, i.e., $E[\mathbf{n}(f)\mathbf{n}^H(f)] = \mathbf{D}(f)$, where $\mathbf{D}(f) = diag[\delta_1(f), \delta_2(f), ..., \delta_M(f)]$, and $\delta_i(f)$ is the noise power for sensor i. The noise power is frequency dependent because high frequency acoustic signatures attenuate faster (more transmission loss) than the low frequency signatures. Using this noise model the covariance matrix of the recorded signal $\mathbf{x}(f)$ becomes $\mathrm{R}_{xx}(f) = \mathbf{a}(f,\theta)\mathbf{a}^H(f,\theta)P_s(f) + \mathbf{D}(f)$. Inserting this into the expression for the theoretical Capon power spectrum (7) and applying the matrix inversion lemma yields

$$P_{\mathrm{Capon}}(f,\theta) = \frac{1}{\Delta - \frac{P_s(f)}{1+P_s(f)\Delta}|\mathbf{a}^H(f,\theta)\mathbf{D}^{-1}(f)\mathbf{a}(f,\theta_0)|^2} \tag{23}$$

where $\Delta = \mathbf{a}^H(f,\theta_0)\mathbf{D}^{-1}(f)\mathbf{a}(f,\theta_0) = \frac{1}{M}\sum_{i=1}^{M}\frac{1}{\delta_i(f)}$. From the formulation of (23) two important consequences of the transmission loss can be observed. First, the overall Capon power spectrum is scaled by the addition of Δ in the denominator of (23). Second, the radiation pattern is now expressed as $P(f,\theta) = |\mathbf{a}^H(f,\theta)\mathbf{D}^{-1}(f)\mathbf{a}(f,\theta_0)|$, i.e., each term in the sum of $P(f,\theta)$ is now weighted by the noise power of the corresponding sensor, thus changing the appearance of the radiation pattern.

In order to implement an accurate transmission loss simulation method, we used the neural network method of acoustic transmission loss prediction described in.[10] This method of transmission loss calculation allows for the incorporation of realistic phenomena experienced by an acoustic signatures propagating in the near ground atmosphere, such as varying source frequencies and problem geometries, refraction or the bending of sound waves due to vertical gradients in wind and temperature, and reflections caused by interactions with the ground. For the presented simulation results we assume baseline environmental parameters (i.e. moderate wind, temperature, and ground conditions). We choose to use the neural network transmission loss calculation method, as opposed to traditional physics-based acoustic models due to the extreme reduction in the computational resources necessary to compute a transmission loss value. Adding acoustic transmission loss in our simulations, or equivalently changing the structure of the noise covariance matrix, causes high frequency target components to introduce more transmission loss than low frequency target components. Large horizontal distances between the target and sensor will also introduce more transmission loss, leading to lower SNR values at those sensors located far from the target.

In the following presented results an array of 15 randomly distributed sensors in a $50\lambda \times 50\lambda$ area is used, with a single source located at θ_0=0 degrees, at a distance of 200m from the center of the array. The source is assumed to be narrowband with a frequency of f=100Hz, and the speed of sound c is set to 335m/s, corresponding to a wavelength of λ=3.35m. The SNR is set to 10dB, and is computed at the sensor in the array which is located closest to the source. All other sensors have lower SNR values, depending on their distance from the source. The transmission loss model also requires the heights of both the source and the sensor, all of which are set at

1m in our experiments. Figure 10(a) shows the radiation pattern of the 15 element randomly distributed sparse array without transmission loss, i.e., $P(f,\theta) = |\mathbf{a}^H(f,\theta)\mathbf{a}(f,\theta_0)|$; while Figure 10(b) shows the radiation pattern of the same sparse array when transmission loss is included, i.e, $P(f,\theta) = |\mathbf{a}^H(f,\theta)\mathbf{D}^{-1}(f)\mathbf{a}(f,\theta_0)|$. Comparing Figures 10(a) and (b) indicates that the main lobe of the radiation pattern has been weakened with respect to the side-lobes once transmission loss is included. We also notice that the shape of the side-lobe structure of the radiation pattern changes between Figures 10(a) and (b) with the inclusion of the transmission loss effects. This is due to the unequal weighting of the elements in the array, caused by the varying values of SNR among different sensors.

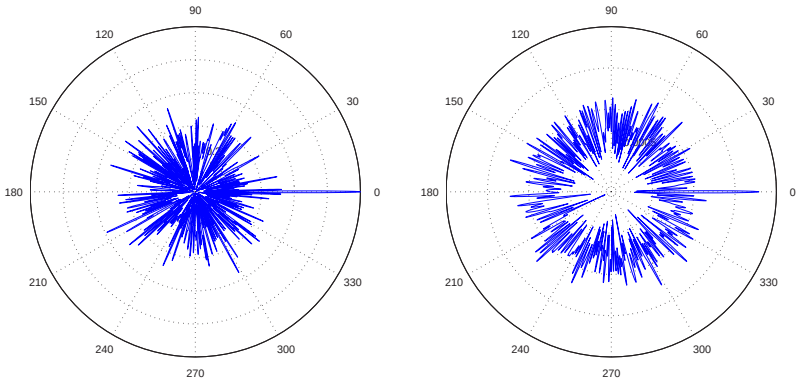

(a) (b)

Figure 10. The radiation pattern $P(f,\theta)$ for 15 randomly distributed microphones in a $50\lambda \times 50\lambda$ surveillance area. (a) Without transmission loss added. (b) With Transmission loss.

Figures 11(a) and (b) show the Capon power spectra of the 15-element randomly distributed sparse array located in a surveillance area of size $50\lambda \times 50\lambda$, without and with the acoustic transmission loss effects, respectively. The effects of acoustic transmission loss on the amplitudes of the main-lobe and the side-lobes are clearly evident from these figures. However, owing to the fact that the randomly distributed sparse arrays exhibit lower side-lobes with no particular structure when compared to the 5-element baseline sparse arrays, the degradation in DOA estimation accuracy as a result of acoustic transmission loss tends to be less severe for these arrays. This important property is clearly noticeable when Figures 11(a) and (b) are compared to the Capon power spectrum for the three 5-element node sparse configurations of Figures 7(a) and (b). Thus, the prominent side-lobe structure of the baseline sparse array configurations can become a major issue in DOA estimation accuracy, especially when transmission loss effects are included.

4. CONCLUSIONS

This paper studied two different sparse acoustic sensor deployment strategies using baseline 5-element arrays as well as randomly distributed microphones. The study of the radiation patterns and bearing responses of these two sparse configurations indicated that the sparse baseline arrays exhibit regular side-lobe structure in their bearing responses. The side-lobes become more prominent when the spacing between the baseline arrays increases. In contrast, the randomly distributed sparse arrays did not show any regular side-lobe structure.

These two configurations were then thoroughly benchmarked in terms of their robustness to various types of model mismatches including sensor location error and fading effects due to acoustic transmission loss. Our results indicated that the distributed sparse arrays remain robust to sensor location uncertainties as long as $\sigma_p < 0.25\lambda$, i.e., the standard deviation of error does not exceed one fourth of the wavelength. Additionally, the robustness improves significantly as the number of sensors in the network increases. The results also attest to the fact that distributed configurations are more immune to transmission loss effects depending on the coverage area.

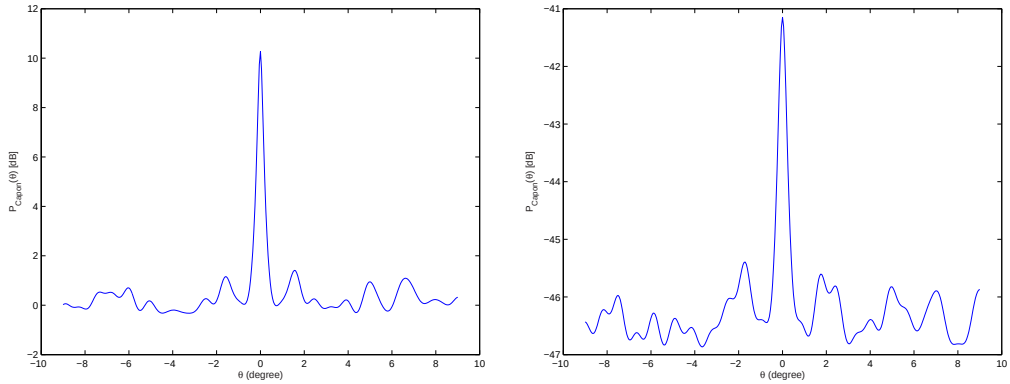

(a) (b)

Figure 11. The Capon power spectrum $P_{\text{Capon}}(f, \theta)$ for 15 randomly distributed microphones in a $50\lambda \times 50\lambda$ area. (a) Without transmission loss added. (b) With Transmission loss.

ACKNOWLEDGMENTS

This work is funded by Army SBIR-Phase II contract # DAAE30-03-C-1055. The data and technical support have been provided by the US Army TACOM-ARDEC, Picatinny Arsenal, NJ. The authors would like to thank Bob Wade and Myron Hohil for their suggestions and technical support.

REFERENCES

1. J. Davis and N. Berry, "Wireless Sensor Network Applications and Impact on MOUT", *Proc. of the SPIE'04 Defense and Security Symposium*, vol. 5417, pp. 435-443, April 2004.
2. M. R. Azimi-Sadjadi, A. Pezeshki, L. L. Scharf and G. Wichern, "Unattended Sparse Acoustic Array Configurations and Beamforming Algorithms," *Proc. of the SPIE'05 Defense and Security Symposium, Unattended Ground Sensors VI*, Vol. 5796, pp.40-51, Orlando, FL, April 2005.
3. K. T. Wong and M. D. Zoltowski, "Direction finding with sparse rectangular dual-size spatial invariance array," *IEEE Trans. on Aerospace Electrn. Syst.*, vol.34, pp. 1320-1327, October 1998.
4. M. D. Zoltowski and K. T. Wong, "Closed-form eigenstructure-based direction finding using arbitrary but identical subarrays on a sparse uniform Cartesian array grid," *IEEE Trans. on Signal Processing*, vol. 48, pp. 2205-2210, August 2000.
5. H. L. Van Trees, *Optimum Array Processing,* Wiley Interscience, 2002.
6. M. R. Azimi-Sadjadi, A. Pezeshki, L. Scharf, and M. Hohil, "Wideband DOA estimation algorithms for multiple target detection and tracking using unattended acoustic sensors," *Proc. of the SPIE'04 Defense and Security Symposium.*, Vol. 5417, pp. 1-11, Orlando, FL, April 2004.
7. Y. T. Lo, "A mathematical theory of antenna arrays with randomly spaced elements," *IRE Trans. Antennas Propagat.*, vol. 12, pp. 257-268, May 1964.
8. H. Ochiai, P. Mitran, H. V. Poor, and V. Tarokh, "Collaborative beamforming in ad hoc networks," *Information Theory Workshop*, San Antonio, TX, October 24-29 2004.
9. G.H. Golub and C.F. Van Loan, *Matrix Computation*, third edition, Johns Hopkins University Press, 1996.
10. G. Wichern, M. R. Azimi-Sadjadi, and M. Mungiole, "Environmentally adaptive acoustic transmission loss prediction using neural networks," *Proc. of the SPIE'05 Defense and Security Symposium*, Vol. 5796, pp.52-61, Orlando, FL, March 2005.